Volume 12
Number 5
7 March 2025
Pages 1357–1678

Materials Horizons

rsc.li/materials-horizons

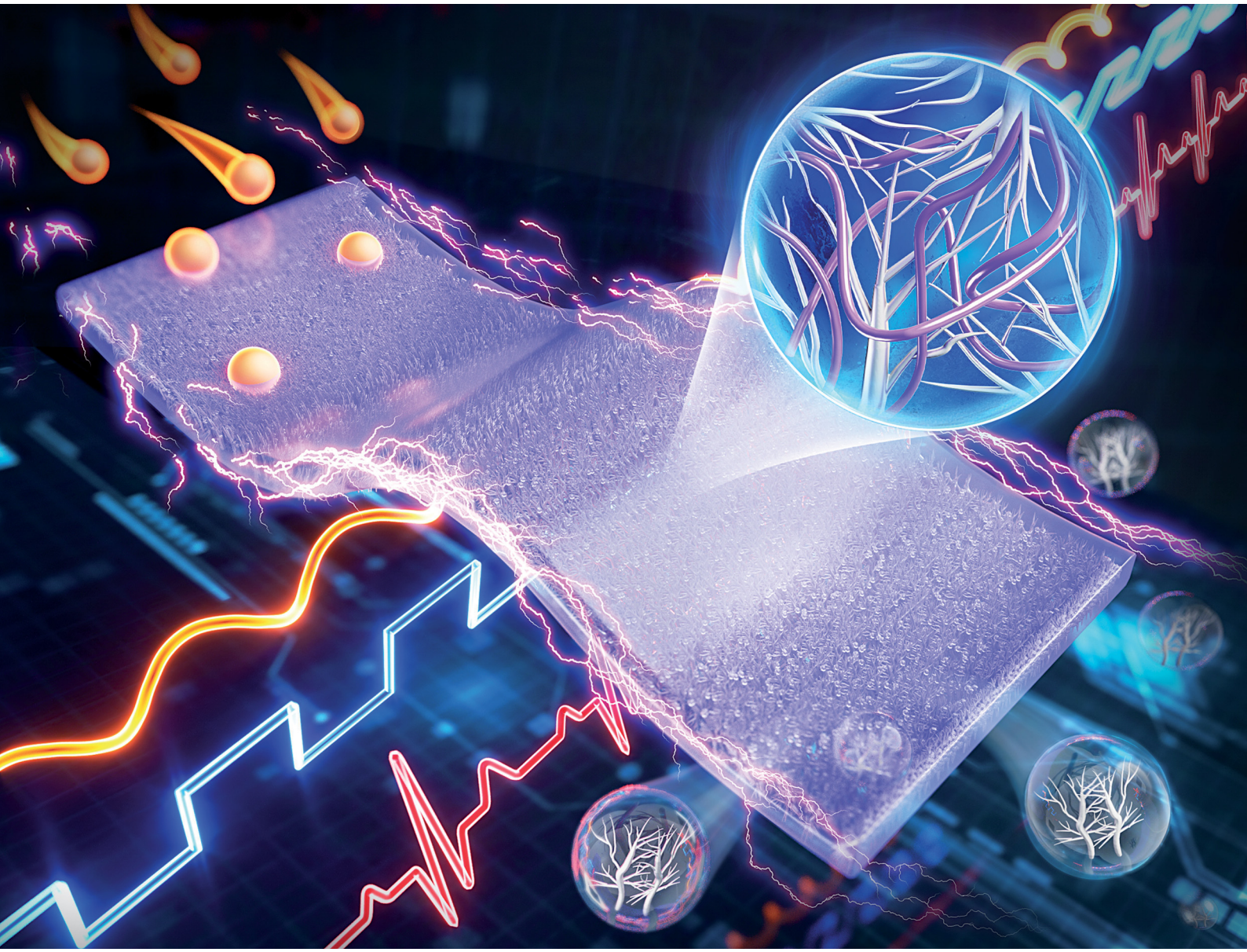

ISSN 2051-6347

ROYAL SOCIETY OF CHEMISTRY

COMMUNICATION

Chen Yu Li, Si Yu Zheng *et al.*

Developing tough, fatigue-resistant and conductive hydrogels *via in situ* growth of metal dendrites

Materials Horizons

ROYAL SOCIETY OF CHEMISTRY

COMMUNICATION

View Article Online
View Journal | View Issue

Cite this: *Mater. Horiz.*, 2025, **12**, 1452

Received 6th December 2024,
Accepted 10th January 2025

DOI: 10.1039/d4mh01778a

rsc.li/materials-horizons

Developing tough, fatigue-resistant and conductive hydrogels *via in situ* growth of metal dendrites†

Mengjie Si,‡[a] Yueman Tang,‡[a] Chen Xu,[a] Chen Yu Li,*[b] Kaishun Xia,[c] Wei Xu,[d] Ji Lin,[e] Zhen Jiang,[f] Jintao Yang[a] and Si Yu Zheng*[a]

Developing hydrogels with high conductivity and toughness *via* a facile strategy is important yet challenging. Herein, we proposed a new strategy to develop conductive hydrogels by growing metal dendrites. Water-soluble Sn^{2+} ions were soaked into the gel and then converted to Sn dendrites *via* an electrochemical reaction; the excessive Sn^{2+} ions were finally removed by water dialysis, accompanied by dramatic shrinkage of the gel. Based on *in situ* transformation from metal ions to dendrites, the method integrated the advantages of ionic conductive fillers, such as LiCl (uniform dispersion), and electrical fillers, such as metal particles (high conductivity). Additionally, the morphology of metal dendrites combined advantages of 1D nanowires (large aspect ratio of the branches) and 2D nanosheets (large specific surface area of the skeleton). The strategy was found to be effective across diverse gel systems (non-ionic, anionic, cationic and zwitterionic). The dense, highly conductive and branched Sn dendrites not only formed a conductive pathway but also interacted with the polymer network to transfer stress and dissipate energy. The resultant gel exhibited a high conductivity of 12.5 S m^{-1}, fracture energy of 1334.0 J m^{-2}, and fatigue threshold of 720 J m^{-2}. Additionally, the gel exhibited excellent sensitivity when used as a wearable strain sensor and bioelectrode. We believe this strategy offers new insights into the development of conductive hydrogels.

New concepts

In this work, a novel strategy to develop conductive hydrogels is proposed by growing metal dendrites within a polymer network *in situ*. Briefly, water-soluble Sn^{2+} ions are soaked into the gel and then converted to Sn dendrites *via* an electrochemical reaction; the excess Sn^{2+} ions in the gel after the reaction are removed through water dialysis. Based on this *in situ* transformation from metal ions to dendrites, the method integrates the advantages of ionic conductive fillers, such as LiCl (uniform dispersion but limited conductivity), and electrical fillers, such as graphene (high conductivity but prone to sedimentation). Moreover, the morphology of metal dendrites combines the advantages of 1D nanowires (large aspect ratio of branches) and 2D nanosheets (large specific surface area of the skeleton). The strategy is effective for various polymer gel systems (non-ionic, anionic, cationic and zwitterionic). The dense and branched Sn dendrites not only form conductive pathways but also interact with the polymer network to transfer stress and dissipate energy. As a result, the mechanical properties and conductivity of the hydrogel are improved simultaneously. We believe this work offers a novel method for constructing conductive and tough hydrogels.

Introduction

Intelligent soft electronics (ISEs) that can interact with humans and environment have attracted great attention in recent years.[1–4] Unlike their rigid counterparts, ISEs can withstand various deformations, such as stretching, bending, folding and twisting, making them suitable for conformal contact and wearability.[5–7] Among diverse soft materials, conductive hydrogels are one of the most suitable candidates for constructing ISEs due to their excellent integration of biocompatibility, stretchability and tissue-like structure.[8–11]

To date, various conductive fillers have been embedded into hydrogels to impart conductivity.[12–16] The fillers can be divided into two types: (1) fillers based on ionic conduction

[a] College of Materials Science & Engineering, Zhejiang University of Technology, Hangzhou 310014, P. R. China. E-mail: zhengsiyu@zjut.edu.cn
[b] Research Center for Humanoid Sensing, Zhejiang Lab, Hangzhou 311100, P. R. China. E-mail: lcyzju@163.com
[c] Department of Orthopedics, The Second Affiliated Hospital, Zhejiang University, Hangzhou, 310009, P. R. China
[d] ZJU-Hangzhou Global Scientific Center, Zhejiang University, Hangzhou 311200, P. R. China
[e] School of Mechanical Engineering & Mechanics, Ningbo University, Ningbo 315211, P. R. China
[f] School of Mechanical Materials, Mechatronic and Biomedical Engineering, University of Wollongong, Wollongong, NSW 2522, Australia

† Electronic supplementary information (ESI) available. See DOI: https://doi.org/10.1039/d4mh01778a

‡ These authors contributed equally to this work.

mechanism, including inorganic salts and ionic liquids;[17–24] (2) fillers based on electric conduction mechanism, including carbon nanomaterials,[25–27] metal nanomaterials[28,29] and conjugated polymers.[30–34] To prepare conductive hydrogels, these conductive fillers are generally dispersed in the monomer precursor with additional ultrasonication treatment before polymerization. However, most electronically conductive fillers are prone to agglomeration or sedimentation in aqueous precursors owing to their inherent hydrophobicity or large particle size, resulting in uneven distribution in the gel and weak filler-matrix interfacial interactions.[35] As a result, additional complex modifications are required to improve the compatibility between the gel and filler.[36] Besides, electronically conductive fillers, such as graphene and conductive polymers, can inevitably deteriorate the stretchability of the gel due to their rigid structure. Some of these fillers even have an obvious negative effect on polymerization.[37] Ionic fillers are usually water soluble and can be facilely soaked into the gel after polymerization, not only securing the reaction but also ensuring uniform dispersion. Unfortunately, the conductivity of ionic hydrogels is generally lower than that of those based on the electrical conduction mechanism. In addition, ions are easily leaked in aqueous environments. Therefore, there is still a need for a facile method to synthesize hydrogels that integrate high conductivity and high toughness.

The uncontrolled growth of metal dendrites is one of the most well-known safety concerns in lithium-ion and aqueous zinc batteries due to the risk of short-circuits.[38] However, from another perspective, the metal dendrite is also a great candidate to develop conductive hydrogels for its high conductivity and ease of growth. Moreover, the morphology of metal dendrites exhibits attractive characteristics and takes advantages of both 1D nanowires (large aspect ratio of the branches) and 2D nanosheets (large specific surface area of the skeleton).[39,40] More importantly, the monomers for growing dendrites, *i.e.*, the metal ions, are water soluble and can be uniformly absorbed into hydrogel just like an ionic filler. Then, the highly conductive metal dendrite can grow *in situ* inside the gel *via* electrochemical reaction. Therefore, it also successfully integrates the advantages of both ionic fillers (uniform dispersion of the initial Sn^{2+} ions) and electrically conductive fillers (high conductivity of the formed Sn dendrites). However, to the best of our knowledge, preparing conductive hydrogels by a relevant strategy is still exclusive and unexplored.

Herein, an *in situ* metal dendrite growth strategy is proposed to prepare conductive and tough hydrogels. Sn^{2+} ions were introduced into the gel by soaking in $SnCl_2$ solution, which

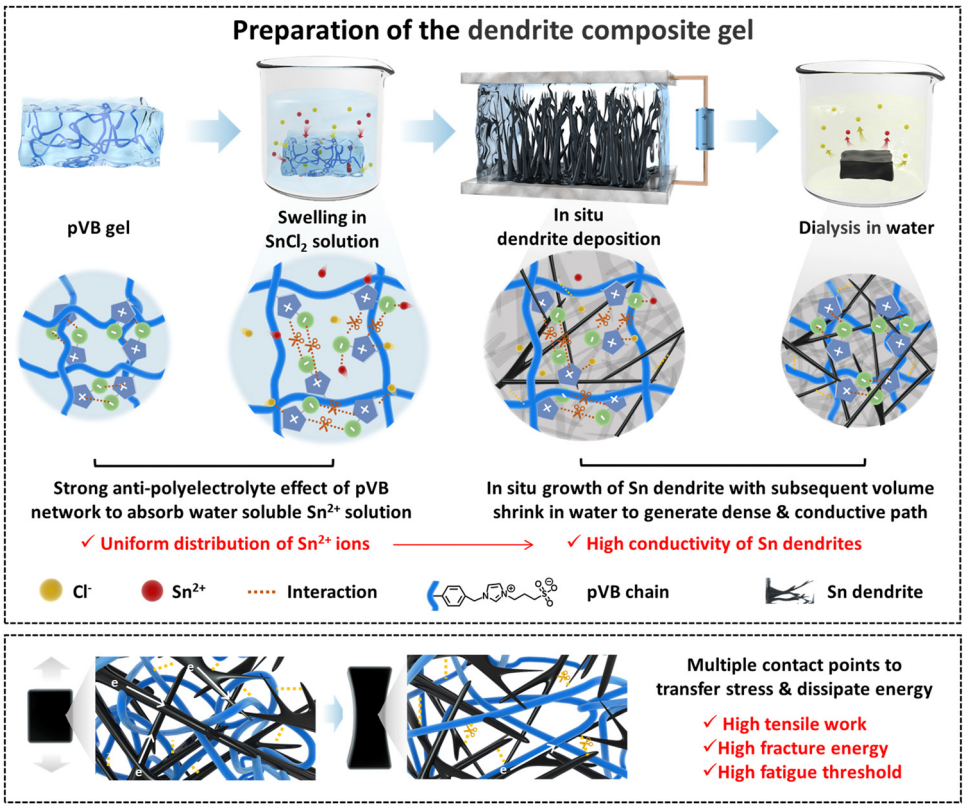

Fig. 1 Design of the dendrite composite gel. The zwitterionic pVB gel absorbs Sn^{2+} ions from $SnCl_2$ solution based on the strong anti-polyelectrolyte effect. Sn electrodes are then attached to both ends of pVB gel to covert Sn^{2+} ions to Sn dendrites *in situ via* an electrochemical reaction. To eliminate excess Sn^{2+} ions, the dendrite composite gel is dialyzed in water. The dense and branched Sn dendrites establish efficient conductive pathways in the gel, resulting in high conductivity. The interactions between the dendrites and pVB chains enable the transfer of stress and dissipation of energy during loading.

were *in situ* converted to Sn dendrites *via* electrochemical reaction; the unreacted Sn^{2+} were dialyzed out of the gel to get the equilibrium gel (Fig. 1). The strategy is effective on diverse polymer gel systems (non-ionic/anionic/cationic/zwitterionic). Meanwhile, zwitterionic poly(3-(1-(4-vinylbenzyl)-1*H*-imidazol-3-ium-3-yl)-propane-1-sulfonate) (pVB) gel shows particularly good performance in Sn^{2+} adsorption and storage due to its strong anti-polyelectrolyte effect.[41] The proposed strategy combines the advantages of traditional ionic filler (uniform dispersion) and electrically conductive filler (high conductivity). The dramatic shrinkage of the gel matrix during the water dialysis process generates dense dendrite network. The highly conductive, branched and ductile Sn dendrites not only contact with each other to form a conductive pathway but contact with pVB chains to transfer stress and dissipate energy. The resultant gel exhibits a high conductivity of 12.5 S m^{-1}, high tensile work of 2.3 MJ m^{-3}, fracture toughness of 1334.0 J m^{-2}, and high fatigue threshold of 720 J m^{-2}. Besides, the dendrite-composited pVB gel exhibits excellent sensitivity when it is applied as a wearable strain sensor and wearable bioelectrode. We believe that the strategy illustrated herein will offer new insights into the development of conductive hydrogels.

Results and discussion

Study of dendrite growth process

To prepare conductive hydrogels, polymer gels are firstly synthesized, which are then immersed in $SnCl_2$ solution to load Sn^{2+} ions. The absorbed Sn^{2+} ions in the gel are *in situ* converted to Sn dendrites *via* the electrochemical reaction. After the formation of the dendrites, the unreacted Sn^{2+} ions are removed out of the gel by immersing the gel in a large amount of water.

To investigate the effect of the polymer structure on the dendrite growth process, several representative polymers were selected to construct the hydrogel (Fig. 2(a)), including pVB

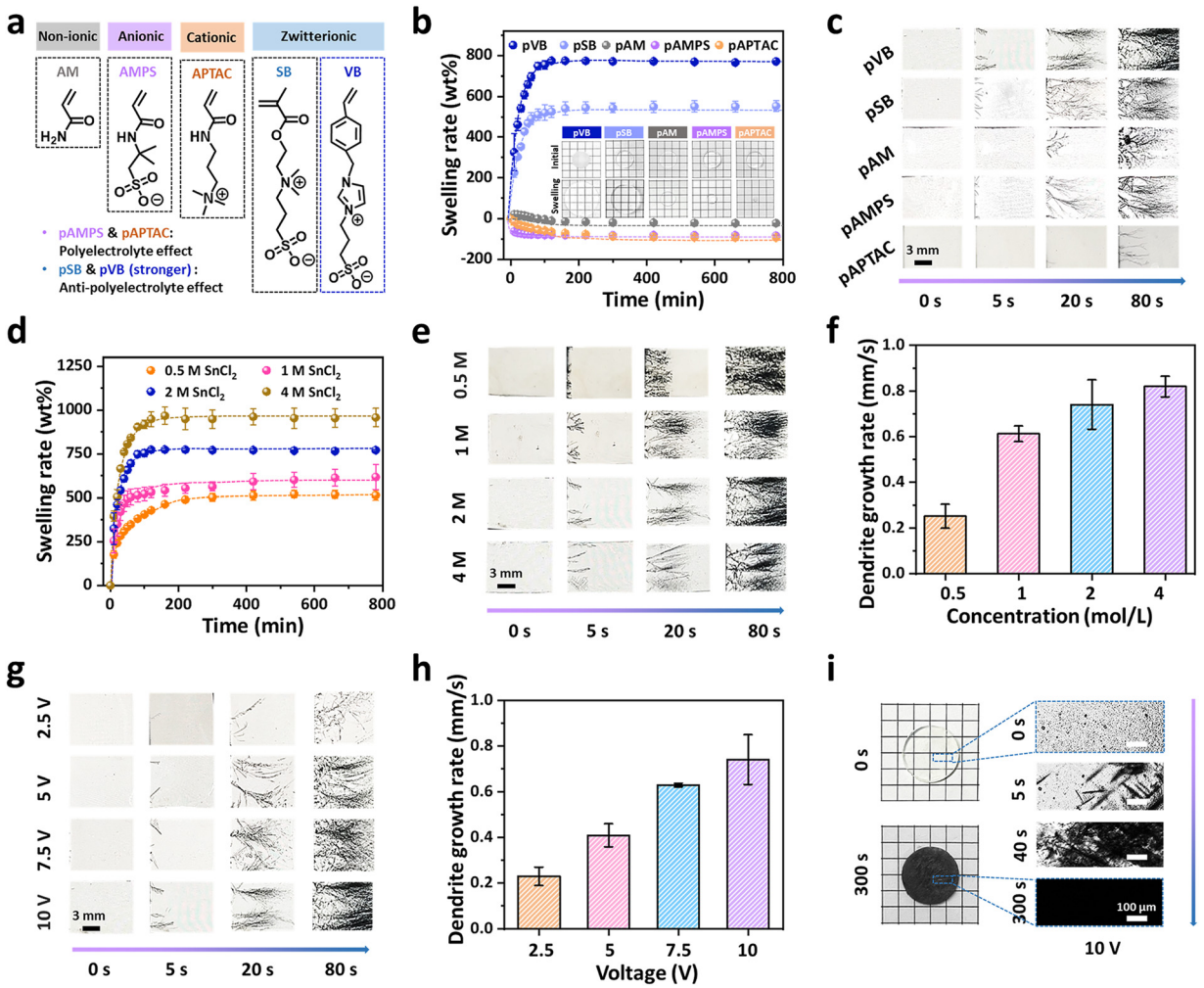

Fig. 2 Study of the dendrite growth process. (a) Molecular structure of the polymer gels, including non-ionic (pAM), anionic (pAMPS), cationic (pAPTAC) and zwitterionic gels (pSB and pVB). (b) Swelling kinetics of different gels in 2 M $SnCl_2$ solution. (c) Photos showing dendrites growth in different gels at 10 V. (d) Swelling dynamics of the pVB gel in $SnCl_2$ solution with varying Sn^{2+} concentrations. (e) Corresponding dendrite growth photos at 10 V and (f) growth rate of dendrites. (g) Dendrite growth images of the pVB gel under different voltage values and (h) corresponding growth rate (2 M $SnCl_2$ solution). (i) Macro- and micro-photos of the pVB gel before and after dendrite deposition.

(zwitterionic polymer with strengthened anti-polyelectrolyte effect), poly(sulfobetaine methacrylate) (pSB, normal zwitterionic polymer), polyacrylamide (pAM, non-ionic polymer), poly(2-acryloylamino-2-methyl-1-propanesulfonic acid) (pAMPS, anionic polymer with polyelectrolyte effect), and poly(3-acrylamidopropyl)trimethylammonium chloride (pAPTAC, cationic polymer with polyelectrolyte effect). As shown in Fig. 2(b), these hydrogels show quite different swelling behavior in $SnCl_2$ solution. The pAMPS and pAPTAC hydrogels shrink in the $SnCl_2$ solution due to the polyelectrolyte effect, while the pAM hydrogel shows negligible volume change in $SnCl_2$ solution due to its non-ionic nature. In contrast, zwitterionic pVB and pSB hydrogels exhibit obvious swelling in $SnCl_2$ solution due to the anti-polyelectrolyte effect; meanwhile, the pVB gel swells more significantly due to its strengthened anti-polyelectrolyte effect originated from the incorporated benzene and imidazole motif.[41] The results indicate that the pVB hydrogel can absorb $SnCl_2$ solution more efficiently. Then, two Sn electrodes are connected to the gel separately and voltage is applied to the gel to trigger the electrochemical reaction (Fig. S1, ESI†). As shown in Fig. 2(c), the Sn dendrites were formed under voltage and the dendrite front gradually moves from the cathode toward the anode. Among these groups, the dendrite in the pVB gel exhibits the most significant proliferation compared to the others, with an apparent growth rate of 0.74 mm s^{-1} (Fig. S2, ESI†). Such rapid proliferation should be attributed to a larger amount of Sn^{2+} solution, which has been absorbed in the pVB gels. It is worth noting that although the dendrite growth rate of pAPTAC is relatively slow, dense dendrite structures can still be grown in the gel by elongating the growth time (Fig. S3, ESI†). Considering the superior performance in growing dendrites, the pVB gel is used in the subsequent study.

The concentration of $SnCl_2$ solution also affects the dendrite growth. As shown in Fig. 2(d), the volume of the pVB gel in $SnCl_2$ solution expands as Sn^{2+} concentration increases, consistent with the general principle of anti-polyelectrolyte effect. A remarkable swelling ratio of 950% is reached for gels equilibrated in 4 M $SnCl_2$ solution (Fig. S4, ESI†). Basically, the growth rate of Sn dendrites in the gel is positively related to the swelling ratio due to the increased nucleating points of the dendrites (Fig. 2(e)).[42,43] The gel equilibrated in 4 M $SnCl_2$ solution exhibits the highest growth rate of 0.82 mm s^{-1} (Fig. 2(f)).

Besides the polymer type and Sn^{2+} concentration, the value of applied voltage affects the dendrite growth. An increase in voltage can promote the electroreduction rate of Sn^{2+} ions and accelerate the growth of Sn dendrites (Fig. 2(g) and (h)). The rapid growth of dendrites may induce more nuclei points, leading to a higher branching degree.[44] The disparity in growth rates under different voltages is further evidenced by snapshots taken after 80 seconds of electrodeposition under a polarizing microscope (Fig. S5, ESI†). After 300 s electrodeposition at 10 V, the pVB hydrogel turns optically black, and microscopic images indicate that the Sn dendrites have completely filled the gel (Fig. 2(i)).

Structure of dendrite composite gels

To remove the residual Sn^{2+} ions, the prepared dendrite composite gels were further immersed in a large volume of water. The gel shrinks obviously after the dialysis of Sn^{2+} ions in water (Fig. 3(a)). The obtained gels are denoted as pVB@*x*Sn, where the *x* refers to the concentration of the previously incubated $SnCl_2$ solution. The scanning electron microscopy (SEM) image of the pVB@4Sn gel reveals the existence of dendrites, which exhibit a squeezed state due to the dramatic shrinkage of the gel matrix (Fig. 3(b)). Elemental mapping further confirms the presence of Sn dendrites, where Sn and C elements show complementary distribution in the images. The crystal structure of the pVB@*x*Sn gel was analyzed by X-ray diffraction (XRD). The XRD result of the pristine pVB gel shows an amorphous character, whereas that of the pVB@4Sn gel exhibits characteristic signals corresponding to the tetragonal crystal structure of Sn dendrites (Fig. 3(c)). The Sn crystallites were mainly oriented to the (101) plane, followed by (200) and (211) planes according to the JCPDS standard card (00-004-0673).[45]

The relative content of Sn dendrite in the gel was then evaluated. Generally, the water content is negatively related to the solid content. The water content of pVB@*x*Sn gels decreases as the Sn^{2+} concentration of solution increases from 0 M to 4 M, indicating an increased Sn dendrite content in the gel (Fig. S6, ESI†). The thermogravimetric results also confirm that the weight content of Sn in the gels increases with the increase in Sn^{2+} concentration (Fig. 3(d)). As the conductive component, the variation of Sn content directly influences the conductivity of the gel. The pVB@*x*Sn gels show much lower resistance compared to that of the pristine pVB gel, whose conductivity increases with an increased amount of Sn dendrite (Fig. 3(e)). Among them, the conductivity of pVB@2Sn and pVB@4Sn gels achieve a high value of 12.5 S m^{-1} and 12.6 S m^{-1}, respectively, which are 730 times greater than that of the pristine pVB gel (Fig. 3(f)). Such high conductivity is originated from three main reasons: (1) the intrinsic high conductivity of Sn metal dendrite, (2) the highly branched structure of dendrite for efficient connection, (3) the highly dense dendrite network generated from the shrinkage of the gel during water dialysis. For the gel matrix with different molecular structures illustrated in Fig. 2(a), all Sn dendrites composite gels exhibit higher conductivity than corresponding pristine ones (without Sn dendrites), demonstrating the effectiveness of the method (Fig. S7, ESI†).

The interaction between Sn dendrite and pVB network was also studied. As shown in Fig. 3(g), the appearance of Sn-related peaks at 486.6 eV and 495.1 eV in the XPS spectrum indicates the successful introduction of Sn dendrites.[46] Meanwhile, the shift of the O–S peak from 533.0 eV to 531.7 eV should be attributed to the formation of interactions between the sulfonate groups of pVB and Sn dendrites (Fig. 3(h)). Besides, such polymer–dendrite interactions were also verified by FTIR spectroscopy, where the character peak of SO_3^- in the pVB@*x*Sn gel exhibits a slight red shift compared to that in the pristine pVB gel (Fig. S8, ESI†).[47]

Mechanical study of pVB@*x*Sn gels

The mechanical performance of the dendrite composite gels was then studied systematically. The dendrite composite pVB hydrogels before water dialysis were highly swollen, brittle and

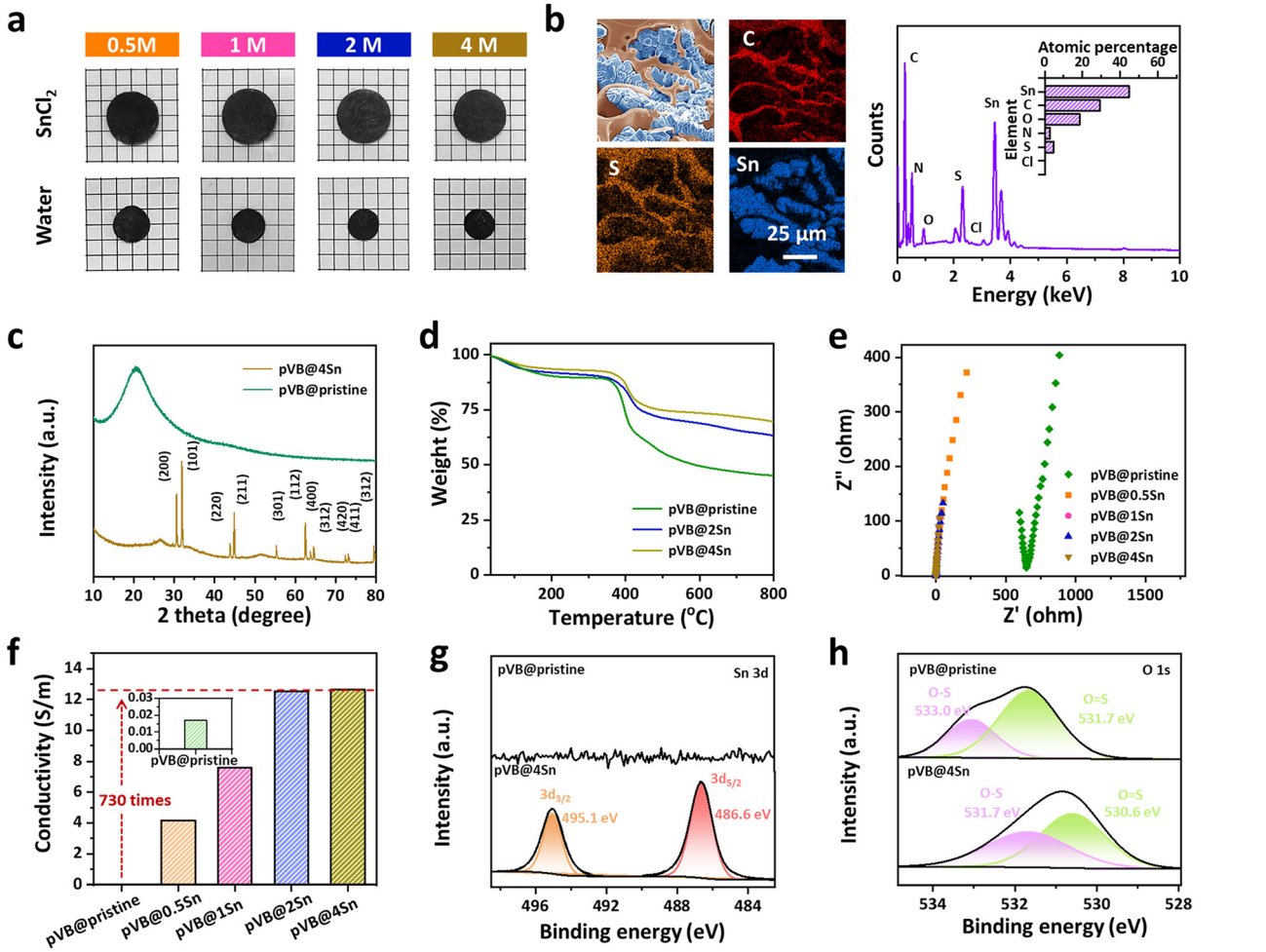

Fig. 3 Structure of dendrite composite gels. (a) Photos of dendrite composite gels equilibrated in $SnCl_2$ solution and those further equilibrated in water. (b) SEM and elemental mapping images of the pVB@4Sn gel, with corresponding elemental analysis. (c) XRD patterns of pVB@4Sn and pVB@pristine gels. (d) Thermogravimetric curves, (e) EIS spectroscopy and (f) conductivity of pVB@*x*Sn gels and pVB@pristine gel. (g) XPS Sn spectra and (h) O spectra of pVB@4Sn gel and pVB@pristine gel.

weak (Fig. S9, ESI†). After removing the residual Sn^{2+} ions in the network, the gels shrink and are much toughened. The tensile curves of the pVB@*x*Sn gels are presented in Fig. 4(a). Basically, the incorporation of Sn dendrites elevates the Young's modulus and tensile work of the gels. This is not only because of the slightly elevated solid content compared to the pristine pVB gel but also the rigid and ductile nature of the incorporated Sn dendrite. Compared to the negligible hysteresis of the pristine pVB gel, the pVB@2Sn gel exhibits a larger hysteresis loop (especially at larger strain) during cyclic loading, demonstrating improved energy dissipation (Fig. 4(b)). The increased dissipated energy in the pVB@2Sn gel should be attributed to the rupture of the interactions between the pVB network and the Sn dendrite. As the ratio of Sn dendrite increases, the Young's modulus of the gel increases from 43 kPa to 592 kPa (Fig. 4(c)). The tensile work of pVB@*x*Sn gels reaches a maximum value of 2.3 MJ m^{-3} when the Sn^{2+} concentration of the incubated solution is 2 M; further increase in the Sn dendrite ratio leads to a decline in the tensile strain and ultimate elongation, probably due to the excessively compact structure (Fig. S10, ESI†). In addition, dendrite composite gels with other polymer structures also show higher tensile strength and tensile work than the corresponding pristine gels, confirming that dendrites can improve the mechanical properties of the gels (Fig. S11, ESI†).

The fracture behavior of pVB@*x*Sn gels was analyzed by single edge notched tensile tests (Fig. S12, ESI†). The fracture toughness of the pVB@*x*Sn gels increases from 370.1 J m^{-2} to 1334.0 J m^{-2} as the Sn^{2+} concentration of the incubated solution increases from 0 M to 2 M (Fig. 4(d)); further increasing the Sn content leads to negligible influence on the fracture toughness. During the stretching of a notched pVB@2Sn gel, obvious crack blunting behavior occurs to impede the crack advancement. The finite element simulation illustrates the strain field within the pVB@2Sn gel under varying levels of strain (Fig. 4(e)). The region ahead of crack tip suffers an obvious stress concentration; the local strain at crack tip achieves 360% as the notched pVB@2Sn gel is stretched to an

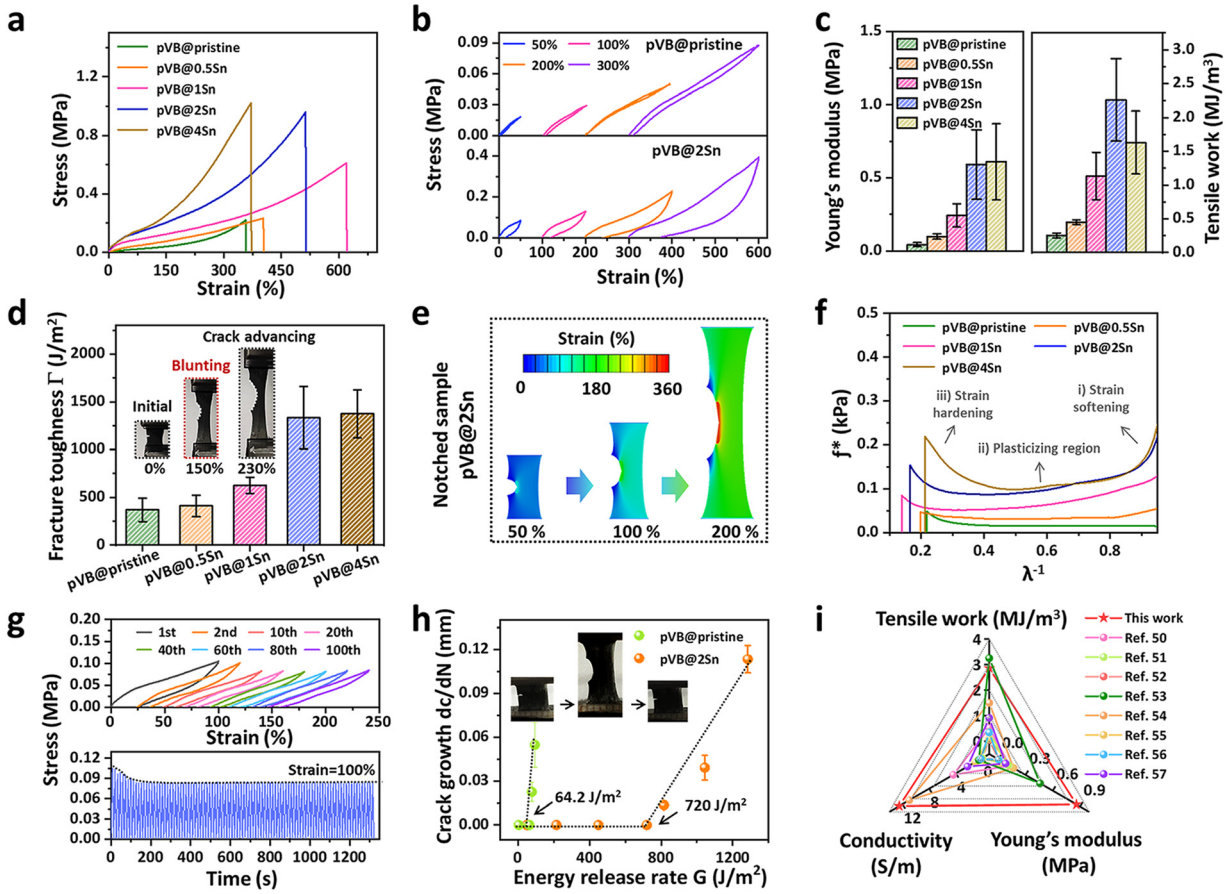

Fig. 4 Mechanical study of pVB@*x*Sn gels. (a) Tensile curves of pVB@*x*Sn gels. (b) Cyclic tensile curves of pristine pVB gel and pVB@2Sn gel at different strains. (c) Young's modulus and tensile work of pVB@*x*Sn gels. (d) Fracture toughness of the pVB@*x*Sn gel; the inset shows the crack evolution of pVB@2Sn gel. (e) Simulated strain field ahead of the crack tip in a notched pVB@2Sn gel. (f) Reduced stress calculation of pVB@*x*Sn gels. (g) Successive 100 cyclic tensile tests of the pVB@2Sn gel at 100% strain and corresponding stress variation during long-term cyclic loading. (h) The fatigue fracture threshold of the pristine pVB gel and pVB@2Sn gel; the inset shows the appearance of a notched pVB@2Sn gel during cyclic loading process. (i) Radar map comparing the pVB@2Sn gel developed here with other reported zwitterionic gel systems.

ultimate strain of 200%. The mechanism for crack resistance is studied through the reduced stress model, where the reduced stress $f^* = \sigma/(\lambda - \lambda^{-2})$ is related to the shear modulus of the material (σ is tensile stress and λ is elongation).[48] The f^*–λ relationship is presented in Fig. 4(f), where the curves undergo three main stages: (1) strain softening region at λ^{-1} of 1–0.83 (0–20% strain), (2) plasticizing region at λ^{-1} of 0.83–0.3 (20–230% strain) and (3) strain hardening region at λ^{-1} of 0.3–0.1 (230–500% strain). At the strain range involving fracture, the f^* level of the pVB@2Sn gel and pVB@4Sn gel is much higher than that of other groups and shows significant strain hardening behavior. Such high local stiffness ahead of crack tip across a wide strain range can impede the crack propagation efficiently. Considering the optimal tensile work and fracture toughness, the pVB@2Sn gel was adopted in the following study.

The cyclic loading behavior of the pVB@2Sn gel was then studied (Fig. 4(g)). Although the pVB@2Sn gel exhibits more noticeable hysteresis compared to the pristine pVB gel, its hysteresis loop area per cycle is relatively stable during long-term cycling at 100% strain. Besides the hysteresis area, the ultimate stress per cycle also remains stable during cycling, securing long-term repeated use. Furthermore, to evaluate the contribution of dendrites to resist crack growth under cyclic loading, the fatigue threshold of the notched gels was investigated.[49] As shown in Fig. 4(h), the fatigue threshold of the pVB@2Sn gel was 720 J m^{-2}, which is 11 times that of the pristine pVB gel. Such improvements in anti-fatigue fracture performance should be attributed to the following reasons: (1) the rigid Sn dendrites aligned ahead of the crack tip can impede the propagation of cracks; (2) the branched dendrites are connected to pVB chains, thereby effectively transferring stress and dissipating energy. The above results show that the introduction of Sn dendrites can simultaneously improve the conductivity and mechanical properties of the gel. Compared with current zwitterionic gel systems,[50–57] the pVB@2Sn gel developed here exhibits outstanding conductivity and mechanical performance, indicating the effectiveness of the strategy (Fig. 4(i)).

pVB@2Sn gel-based sensor

To demonstrate the potential application of conductive gels developed by the dendrite growth strategy, the pVB@2Sn gel

was encapsulated by VHB tapes to construct a resistive strain sensor (Fig. S13, ESI†). Interestingly, the pVB@2Sn gel sensor shows a high gauge factor (GF) of 4.5 at 0–100% strain, 12.0 at 100–200% strain and 24.4 at 200–250% strain, demonstrating high sensitivity to strain (Fig. 5(a)). The strain–resistance relationship of the pVB@2Sn gel deviated from the theoretical prediction of ideal polymer systems ($\Delta R/R_0 = \varepsilon^2 + 2\varepsilon$), which should be attributed to the incorporation of Sn dendrites.[40] The contact points of neighbouring branches would be separated under strain and contact again after resilience, leading to reversible cut-off and connection of the conductive pathway. The strain sensitivity (GF) of the pVB@2Sn gel sensor achieved here exceeds many existed gel-based strain sensors (Fig. 5(b)).[58–61] Furthermore, the response time and recovery time of the pVB@2Sn gel to 20% strain were 0.2 s and 0.24 s, respectively (Fig. S14, ESI†). Besides the sensitivity, both of the unnotched and notched pVB@2Sn gel sensors, exhibit delicate and repeatable signals when switching the applied strain between 5% and 100% (Fig. 5(c) and Fig. S15, ESI†). To study the signal stability during long-term cycling, 200 successive cyclic loading is performed on the pVB@2Sn gel sensor at 50% strain. As shown in Fig. 5(d), the resistive signal does not show significant attenuation during the cycling. To reveal the reason for the good cycling performance, the deformation process of

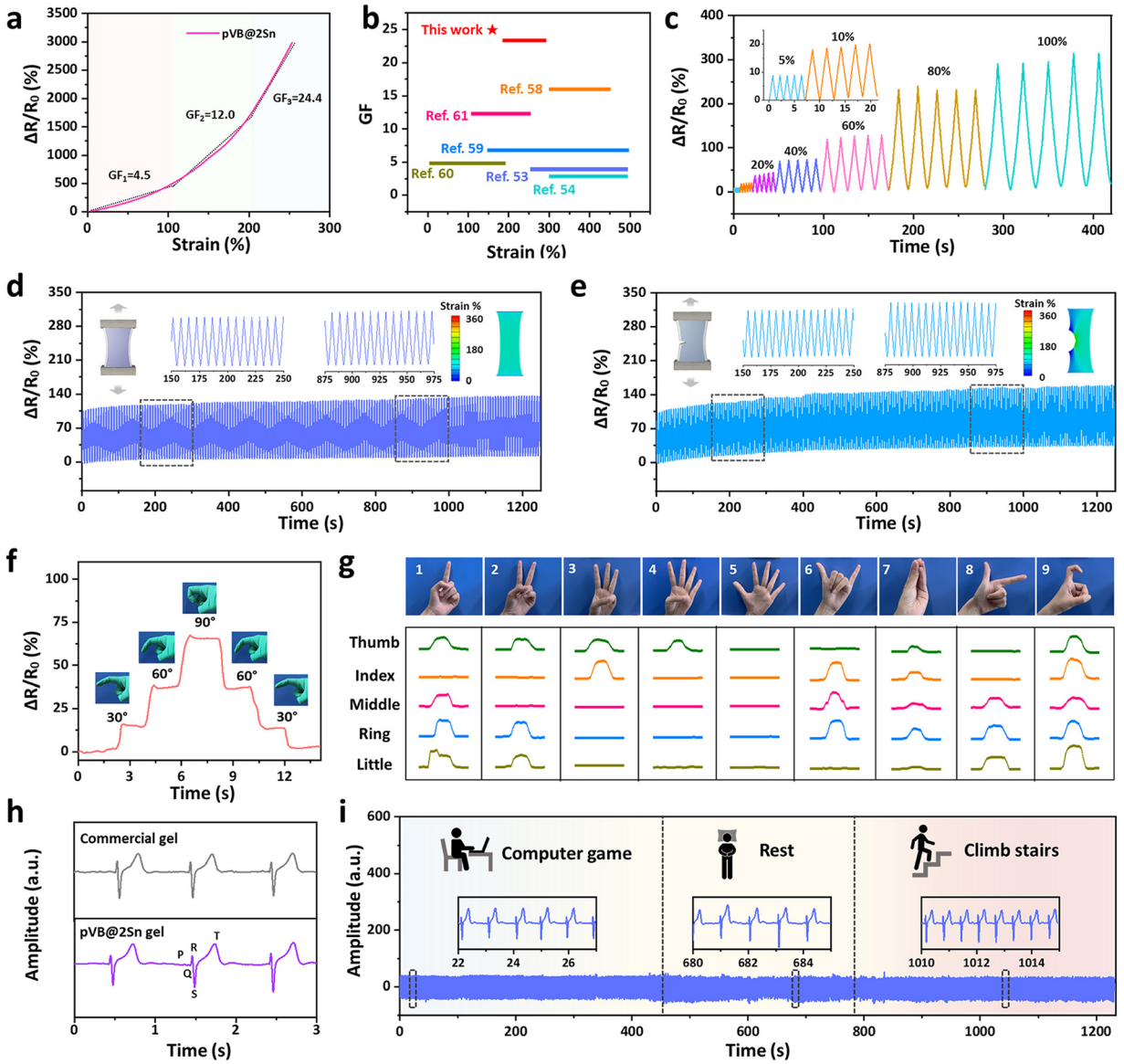

Fig. 5 pVB@2Sn gel-based sensor. (a) The resistive signal of the pVB@2Sn sensor in response to applied strain. (b) Comparison of the pVB@2Sn gel sensor with existing zwitterionic gel-based sensors. (c) The resistive signal of the pVB@2Sn gel sensor under different strains ranging from 5% to 100%. (d) and (e) The long-term cycling performance of sensors based on pVB@2Sn gels: (d) without and (e) with crack under 200 successive cyclic loadings at 50% strain; the insets show the simulated strain field. (f) and (g) Monitoring the (f) bending angle of a single finger and (g) complex gestures. (h) The ECG signals recorded in the supine position using bioelectrodes based on commercial conductive gel and pVB@2Sn gel. (i) ECG signals recorded by a pVB@2Sn gel bioelectrode during various daily activities (static and dynamic).

dendrites was observed directly under a microscope. It was found that the displaced Sn dendrites during loading can almost return to their original position after removing the load, indicating the good resilience of the dendrite network (Fig. S16, ESI†). Furthermore, the cycling test of a notched pVB@2Sn gel sensor was also performed. As shown in Fig. 5(e), the intensity of the resistive signal obtained from the notched pVB@2Sn gel sensor is comparable to that from the un-notched one, with no obvious signal deviation during 200 cycles, thus highlighting the crack insensitivity of the pVB@2Sn gel.

To illustrate the capability of the sensor in recognizing real human movement, the pVB@2Sn gel sensor was applied to finger joints. As shown in Fig. 5(f), the bending action of the finger can be well detected by the sensor. As the bending angle increases from 30° to 60° and to 90°, the corresponding signal increases from 15.1% to 37.1% and to 65.5%, respectively; reverse changes of the bending angles can also be recognized. Notably, more complex gesture recognition can be realized by conducting multiple signals from five fingers simultaneously. As presented in Fig. 5(g), the gestures representing 1 to 9 can be accurately identified by the sensors. Besides monitoring human actions, two separated sensors were installed inside and outside of a mechanical gripper to recognize the grasping action. Signals corresponding to the internal and external deformation of the gripper were generated simultaneously to identify the actions of grasping or releasing (Fig. S17, ESI†).

Besides strain sensors, the remarkable electrical conductivity of the pVB@2Sn gels render them promising candidates for bioelectrodes. As a long-term contact device, the pVB@2Sn gel also has good biocompatibility to prevent inflammation (Fig. S18, ESI†). The pVB@2Sn gel was assembled into a bioelectrode and then affixed on the wrist to monitor electrophysiological (ECG) signals (Fig. S19, ESI†). As illustrated in Fig. 5(h), the ECG signal recorded by the pVB@2Sn bioelectrode exhibits typical QRS, P and T waves comparable to those obtained from commercial electrodes. Besides, the pVB@2Sn bioelectrode shows a higher signal-to-noise ratio of 38.6 dB compared to that of commercial electrodes (36.3 dB). Furthermore, both static and dynamic ECG signals during various activities can be effectively detected by equipping with the pVB@2Sn bioelectrode, including playing computer games, climbing stairs, and resting (Fig. 5(i)). All of these results highlight the potential for the development of pVB@2Sn gels in facilitating human health monitoring and physiological medical diagnosis.

Conclusions

In this work, we developed a strategy for preparing conductive hydrogels by growing metal dendrite inside the gel. Water-soluble Sn^{2+} ions were soaked into the gel and then transformed into Sn dendrites *in situ*. The method integrates the typical advantages of ionic additive (uniform dispersion of original Sn^{2+} ions) and electrical filler (high conductivity of the formed Sn dendrites). The strong anti-polyelectrolyte effect of the pVB gel network promotes the adsorption of Sn^{2+} ions, contributing to the efficient growth of Sn dendrites. The branched and ductile Sn dendrites not only form a highly connected conductive pathway to impart conductivity but also contact with pVB chains to transfer stress and dissipate energy. The resultant hydrogels show outstanding conductivity (12.5 S m^{-1}), high tensile work (2.3 MJ m^{-3}), fracture toughness (1334.0 J m^{-2}) and high fatigue fracture threshold (720 J m^{-2}). Besides, the pVB@2Sn gel is assembled into a wearable strain sensor and bioelectrode to demonstrate its potential use, which exhibits high sensitivity and high signal-to-noise ratio. We believe that this work can offer new insights into the development of conductive hydrogels.

Experimental

Materials

Hydrochloric acid was supplied by Sinopharm Chemical Reagent Co., Ltd. 4-Vinylbenzyl chloride, 2959, $SnCl_2$, *N*,*N*-methylene-bis-acrylamide (MBAA), 2-acryloylamino-2-methyl-1-propanesulfonic acid (AMPS), (3-acrylamidopropyl) trimethylammonium chloride (APTAC), and SB were purchased from Aladdin Biochemical Technology Co., Ltd. VHB tape was purchased from 3M Co., Ltd. Fetal bovine serum and penicillin–streptomycin solution were purchased from Beyotime Biotechnology Co., Ltd. Monomer of VB was synthesized using the methods from our previous work.[6]

Synthesis of gel

The precursor of the gel was composed of water, 2959, MBAA and monomer (ESI,† Table S1). The precursor was injected into a mold made of two glass plates and a Teflon mold, then exposed to 365 nm ultraviolet light for 4 hours. The obtained gel was immersed in water for 24 h to remove the unreacted species. $SnCl_2$ was dissolved in water containing 1 M hydrochloric acid to create $SnCl_2$ solutions with varying concentrations. The gel was immersed in $SnCl_2$ solutions for 24 h for Sn^{2+} loading; then, the gel was picked out and Sn metal electrodes were attached to both ends of the gel. A DC power source was connected (KORAD KA3005D) to apply direct current to grow Sn dendrites under certain voltages (2.5 V, 5 V, 7.5 V, and 10 V) for a certain time. After that, the obtained gel was equilibrated in water for another 24 h to remove residual Sn^{2+} ions.

Characterization

Dendrite growth was observed using a metallographic microscope (CX40M). The apparent growth rate of dendrites was calculated by $v = \Delta L/t$, where ΔL represents the growth distance of the dendrite front recorded after a specified duration t (the electrode spacing is 20 mm). The structure of Sn dendrite in the gel was determined by X-ray diffraction (XRD, Rigaku Smart Lab SE). The chemical information of the gels was analyzed by Fourier transform infrared spectroscopy (FTIR, Nicolet 6700) and X-ray photoelectron spectroscopy (XPS, Thermo Scientific K-Alpha Nexsa spectrometer). The morphology and elemental analysis of the gel were determined by a cold field emission

scanning electron microscope (Hitachi S4700). The thermal decomposition of the gel was measured by a thermogravimeter (HITACHI STA200), with the tested temperature range of 0–800 °C and heating rate of 20 °C min^{-1}.

Mechanical test

The mechanical properties of the gels were tested using a universal testing machine (Instron 5966), with a tensile rate of 50 mm min^{-1}. For fracture test, a 1.5 mm crack was created on one side of a 5 × 6 mm rectangular gel sample, and the sample was then subjected to uniaxial stretching in order to test its resistance to crack propagation. The calculation of fracture energy of the gel followed the typical formula of single edge notched tests. To determine the fatigue fracture threshold, the specimen with same geometry were subjected to cyclic loading at different strains, and crack growth per cycle was recorded.

Cytotoxicity test

The pVB@2Sn gel was immersed in 75% alcohol and subsequently washed 3 times with PBS solution. The gel was then placed in a medium containing 1% penicillin–streptomycin solution and incubated at 37 °C for 24 h. The gel extract was filtered through a bacteria-retentive filter with a pore size of 0.22 μm. Following this, PC-12 cells were implanted in 6-well plates with a gel extract containing 10% fetal bovine serum and 1% penicillin–streptomycin solution and cultured at 37 °C for 24 h. The control group was incubated with PC-12 cells using a medium containing 10% fetal bovine serum and 1% penicillin–streptomycin solution. Subsequently, the cells were stained in darkness for 20 minutes, after which live/dead staining was done using a fluorescence microscope.

Electrical test

To test the sensing properties of the gel, it was bound with copper tape at both ends and connected to an electrochemical workstation (CHI 760E). VHB tape was used to encapsulate the gel to prevent water loss. The packaging gel was subjected to a tensile test using a universal testing machine and an electrochemical workstation. The corresponding change in the resistance was determined according to the formula

$$\Delta R/R_0 = (R - R_0)/R_0 \times 100\% \quad (1)$$

where R_0 is the initial resistance of the gel before testing and R is the real-time resistance of the gel at various strains. To further test the strain response of the gel, the gel was applied to human fingers and mechanical claws.

The ECG signals were recorded using an ADS129x (Texas Instruments). The conductive gel in commercial Ag/AgCl electrodes was replaced by pVB@2Sn gel to monitor ECG signals. The SNR (dB) is defined by the formula $SNR = 20 \times \log_{10}(V_s/V_n)$, where V_s represents the amplitude of the signal peak and V_n denotes the background amplitude. The test subject was a male at age of 20 who took part under informed consent.

Finite element simulation

We used the finite element software ABAQUS to simulate the tension of the notched gel samples and visualized the strain deformation. The gel was simplified as a two-dimensional membrane, described by the eight-chain model. The geometries of the simulation were set to match those of the experiments. Different displacements were applied to the upper end of the gel to simulate various tensile strains, while the lower end was fixed to prevent movement.

Author contributions

M. S. performed experiments, analyzed the results and wrote the manuscript. Y. T. participated in data analysis and paper writing. C. X. participated in the experiment of the sensor. J. L. performed simulation calculations. K. X., W. X., Z. J., and J. Y. provided opinion on the work. S. Y. Z. and C. Y. L. constructed the idea, supervised the work and revised the manuscript.

Data availability

The data supporting the findings of this study are available from the corresponding author upon reasonable request.

Conflicts of interest

The authors declare no competing interests.

Acknowledgements

C. Y. Li thanks the support from the National Natural Science Foundation of China (no. 52303161). S. Y. Z. thanks the support from the National Natural Science Foundation of China (no. 52473022 and 52203073) and from the Natural Science Foundation of Zhejiang Province (no. LY24E030011). J. Y. acknowledges the support from the National Natural Science Foundation of China (no. 52073255 and 51673175).

References

1 Z. Liu, X. Hu, R. Bo, Y. Yang, X. Cheng, W. Pang, Q. Liu, Y. Wang, S. Wang, S. Xu, Z. Shen and Y. Zhang, *Science*, 2024, **384**, 987–994.
2 Q. Zhuang, K. Yao, C. Zhang, X. Song, J. Zhou, Y. Zhang, Q. Huang, Y. Zhou, X. Yu and Z. Zheng, *Nat. Electron.*, 2024, **7**, 598–609.
3 S. H. Kim, A. Basir, R. Avila, J. Lim, S. W. Hong, G. Choe, J. H. Shin, J. H. Hwang, S. Y. Park, J. Joo, C. Lee, J. Choi, B. Lee, K.-S. Choi, S. Jung, T.-I. Kim, H. Yoo and Y. H. Jung, *Nature*, 2024, **629**, 1047–1054.
4 D. Wang, D. Liu, J. H. Xu, J. J. Fu and K. Wu, *Mater. Horiz.*, 2022, **9**, 640–652.
5 H. Wang, B. Liu, D. Chen, Z. Wang, H. Wang, S. Bao, P. Zhang, J. Yang and W. Liu, *Mater. Horiz.*, 2024, **11**, 2628–2642.

6 S. Y. Zheng, S. Mao, J. Yuan, S. Wang, X. He, X. Zhang, C. Du, D. Zhang, Z. L. Wu and J. Yang, *Chem. Mater.*, 2021, **33**, 8418–8429.
7 H. Lin, D. Zheng, X. Wu, R. He, L. He, X. Zhou, H. Zuo, C. Yuan, B. Zeng, Y. Xu and L. Dai, *Sci. Adv.*, 2024, **10**, eadp0730.
8 H. Fu, B. Wang, J. Li, J. Xu, J. Li, J. Zeng, W. Gao and K. Chen, *Mater. Horiz.*, 2022, **9**, 1412–1421.
9 Y. Shin, H. S. Lee, Y. J. Hong, S. H. Sunwoo, O. K. Park, S. H. Choi, D. H. Kim and S. Lee, *Sci. Adv.*, 2024, **10**, eadi7724.
10 J. Lin, X. Chen, P. Zhang, Y. Xue, Y. Feng, Y. Feng, Z. Ni, Y. Tao, Y. Wang and J. Liu, *Adv. Mater.*, 2024, **36**, 2400181.
11 X. Di, J. Hou, M. Yang, G. Wu and P. Sun, *Mater. Horiz.*, 2022, **9**, 3057–3069.
12 T. Zhu, Y. Ni, G. M. Biesold, Y. Cheng, M. Ge, H. Li, J. Huang, Z. Lin and Y. Lai, *Chem. Soc. Rev.*, 2023, **52**, 473–509.
13 Q. Xia, W. Li, X. Zou, S. Zheng, Z. Liu, L. Li and F. Yan, *Mater. Horiz.*, 2022, **9**, 2881–2892.
14 Q. Zhang, H. Lu, G. Yun, L. Gong, Z. Chen, S. Jin, H. Du, Z. Jiang and W. Li, *Adv. Funct. Mater.*, 2023, **34**, 2308113.
15 X. Li, M. Jiang, Y. Du, X. Ding, C. Xiao, Y. Wang, Y. Yang, Y. Zhuo, K. Zheng, X. Liu, L. Chen, Y. Gong, X. Tian and X. Zhang, *Mater. Horiz.*, 2023, **10**, 2945–2957.
16 G. Chen, Y. Zhang, S. Li, J. Zheng, H. Yang, J. Ren, C. Zhu, Y. Zhou, Y. Chen and J. Fu, *Adv. Mater.*, 2024, **36**, 2408193.
17 Z. Yu and P. Wu, *Mater. Horiz.*, 2021, **8**, 2057–2064.
18 J. Ren, G. Chen, H. Yang, J. Zheng, S. Li, C. Zhu, H. Yang and J. Fu, *Adv. Mater.*, 2024, **36**, 2412162.
19 X. Sui, H. Guo, P. Chen, Y. Zhu, C. Wen, Y. Gao, J. Yang, X. Zhang and L. Zhang, *Adv. Funct. Mater.*, 2020, **30**, 1907986.
20 Y. H. Ye, B. Wu, S. Sun and P. Wu, *Adv. Mater.*, 2024, **36**, 2402501.
21 J. Wei, Y. Zheng and T. Chen, *Mater. Horiz.*, 2021, **8**, 2761–2770.
22 H. Wang, A. Zhou, Z. Hu, X. Hu, F. Zhang, Z. Song, Y. Huang, Y. Cui, Y. Cui, L. Li, F. Wu and R. Chen, *Angew. Chem., Int. Ed.*, 2024, **63**, e202318928.
23 C. Dai, Y. Wang, Y. Shan, C. Ye, Z. Lv, S. Yang, L. Cao, J. Ren, H. Yu, S. Liu, Z. Shao, J. Li, W. Chen and S. Ling, *Mater. Horiz.*, 2023, **10**, 136–148.
24 H. Xiang, X. Li, B. Wu, S. Sun and P. Wu, *Adv. Mater.*, 2023, **35**, 2209581.
25 G. F. Cai, J. X. Wang, K. Qian, J. W. Chen, S. H. Li and P. S. Lee, *Adv. Sci.*, 2017, **4**, 1600190.
26 K. B. C. Imani, J. M. Dodda, J. Yoon, F. G. Torres, A. B. Imran, G. R. Deen and R. Al-Ansari, *Adv. Sci.*, 2024, **11**, 2306784.
27 J. Deng, H. Yuk, J. Wu, C. E. Varela, X. Chen, E. T. Roche, C. F. Guo and X. Zhao, *Nat. Mater.*, 2021, **20**, 229–236.
28 X. Wang, S. Zheng, J. Xiong, Z. Liu, Q. Li, W. Li and F. Yan, *Adv. Mater.*, 2024, **36**, 2313845.
29 K. Yang, Q. Li, S. Tian, J. Wang, G. Lu, H. Guo, S. Xu, L. Zhang and J. Yang, *J. Am. Chem. Soc.*, 2024, **146**, 10699–10707.
30 Y. Ohm, C. Pan, M. J. Ford, X. Huang, J. Liao and C. Majidi, *Nat. Electron.*, 2021, **4**, 185–192.
31 M. Leng, N. Koripally, J. Huang, A. Vriza, K. Y. Lee, X. Ji, C. Li, M. Hays, Q. Tu, K. Dunbar, J. Xu, T. N. Ng and L. Fang, *Mater. Horiz.*, 2023, **10**, 4354–4364.
32 W. W. Deng, Z. P. Zhang, M. Z. Rong and M. Q. Zhang, *Mater. Horiz.*, 2024, **11**, 4507–4518.
33 D. Won, J. Kim, J. Choi, H. J. Kim, S. Han, I. Ha, J. Bang, K. K. Kim, Y. Lee, T.-S. Kim, J.-H. Park, C.-Y. Kim and S. H. Ko, *Sci. Adv.*, 2022, **8**, eabo3209.
34 T. Zhou, H. Yuk, F. Hu, J. Wu, F. Tian, H. Roh, Z. Shen, G. Gu, J. Xu, B. Lu and X. Zhao, *Nat. Mater.*, 2023, **22**, 895–902.
35 T. Li, H. Qi, Y. Zhao, P. Kumar, C. Zhao, Z. Li, X. Dong, X. Guo, M. Zhao, X. Li, X. Wang, R. O. Ritchie and W. Zhai, *Sci. Adv.*, 2024, **10**, eadk6643.
36 H.-Y. Chen, Z.-Y. Chen, M. Mao, Y.-Y. Wu, F. Yang, L.-X. Gong, L. Zhao, C.-F. Cao, P. Song, J.-F. Gao, G.-D. Zhang, Y.-Q. Shi, K. Cao and L.-C. Tang, *Adv. Funct. Mater.*, 2023, **33**, 2304927.
37 G. Li, C. Li, G. Li, D. Yu, Z. Song, H. Wang, X. Liu, H. Liu and W. Liu, *Small*, 2022, **18**, 2101518.
38 L.-F. Zhou, T. Du, J.-Y. Li, Y.-S. Wang, H. Gong, Q.-R. Yang, H. Chen, W.-B. Luo and J.-Z. Wang, *Mater. Horiz.*, 2022, **9**, 2722–2751.
39 K. Guo, D. Xu, L. Xu, Y. Li and Y. Tang, *Mater. Horiz.*, 2023, **10**, 1234–1263.
40 I. K. Han, K.-I. Song, S.-M. Jung, Y. Jo, J. Kwon, T. Chung, S. Yoo, J. Jang, Y.-T. Kim, D. S. Hwang and Y. S. Kim, *Adv. Mater.*, 2023, **35**, 2203431.
41 S. Y. Zheng, J. Zhou, M. Si, S. Wang, F. Zhu, J. Lin, J. Fu, D. Zhang and J. Yang, *Adv. Funct. Mater.*, 2023, **33**, 2303272.
42 Y. Xiong, B. Yan, Q. Li, C. Zhi and J. Fan, *J. Power Sources*, 2024, **597**, 234162.
43 Z. Wang, Z. Sun, J. Li, Y. Shi, C. Sun, B. An, H. M. Cheng and F. Li, *Chem. Soc. Rev.*, 2021, **50**, 3178–3210.
44 Z. Wang, J. Ru, Y. Hua, J. Bu, X. Geng and W. Zhang, *J. Solid State Electrochem.*, 2021, **25**, 1111–1120.
45 M. Wang, C. Jiang, S. Zhang, X. Song, Y. Tang and H.-M. Cheng, *Nat. Chem.*, 2018, **10**, 667–672.
46 J. Liu, H. Yao, S. Wang, C. Wu, L. Ding and F. Hao, *Adv. Energy Mater.*, 2023, **13**, 2300696.
47 Y. Tang, M. Si, Y. J. Wang, J. Zhou, Y. Deng, K. Xia, Z. Jiang, D. Zhang, S. Y. Zheng and J. Yang, *Adv. Sci.*, 2024, **11**, 2407501.
48 M. Si, X. Jian, Y. Xie, J. Zhou, W. Jian, J. Lin, Y. Luo, J. Hu, Y. J. Wang, D. Zhang, T. Wang, Y. Liu, Z. L. Wu, S. Y. Zheng and J. Yang, *Adv. Energy Mater.*, 2024, **14**, 2303991.
49 S. Han, Q. Wu, J. Zhu, J. Zhang, A. Chen, S. Su, J. Liu, J. Huang, X. Yang and L. Guan, *Mater. Horiz.*, 2023, **10**, 1012–1019.
50 J. Ren, Y. Liu, Z. Wang, S. Chen, Y. Ma, H. Wei and S. Lü, *Adv. Funct. Mater.*, 2022, **32**, 2107404.
51 X. Pei, H. Zhang, Y. Zhou, L. Zhou and J. Fu, *Mater. Horiz.*, 2020, **7**, 1872–1882.
52 S. Hao, L. Meng, Q. Fu, F. Xu and J. Yang, *Chem. Eng. J.*, 2022, **431**, 133782.

53 Y. Zhang, T. Li, L. Miao, P. Kaur, S. Men, Q. Wang, X. Gong, Y. Fang, C. Zhai, S. Zhang, L. Zhang and L. Ye, *J. Mater. Chem. A*, 2022, **10**, 3970–3988.
54 Q. Jiao, L. Cao, Z. Zhao, H. Zhang, J. Li and Y. Wei, *Biomacromolecules*, 2021, **22**, 1220–1230.
55 Z. Zhang, A. Yao and P. Raffa, *Adv. Funct. Mater.*, 2024, **34**, 2407529.
56 K. He, P. Cai, S. Ji, Z. Tang, Z. Fang, W. Li, J. Yu, J. Su, Y. Luo, F. Zhang, T. Wang, M. Wang, C. Wan, L. Pan, B. Ji, D. Li and X. Chen, *Adv. Mater.*, 2024, **36**, 2311255.
57 X. Liu, X. Ji, R. Zhu, J. Gu and J. Liang, *Adv. Mater.*, 2024, **36**, 2309508.
58 D. Pei, S. Yu, X. Zhang, Y. Chen, M. Li and C. Li, *Chem. Eng. J.*, 2022, **445**, 136741.
59 L. Zhao, B. Wang, Z. Mao, X. Sui and X. Feng, *Chem. Eng. J.*, 2022, **433**, 133500.
60 W. Y. Guo, T. Mai, L. Z. Huang, W. Zhang, M. Y. Qi, C. Yao and M. G. Ma, *ACS Appl. Mater. Interfaces*, 2023, **15**, 24933–24947.
61 Y. He, S. Sun, X. Zhang, Y. Xu, C. Zhang, C. Shao, J. Yang and J. Wen, *ACS Sustainable Chem. Eng.*, 2024, **12**, 11809–11820.

